

FORMATION OF MAGNETIC FLUX ROPE DURING SOLAR ERUPTION. I. EVOLUTION OF TOROIDAL FLUX AND RECONNECTION FLUX

CHAOWEI JIANG¹, JUN CHEN^{2,3}, AIYING DUAN⁴, XINKAI BIAN¹, XINYI WANG⁵, JIAYING LI¹, PENG ZOU¹, XUESHANG FENG^{1,5}

¹Institute of Space Science and Applied Technology, Harbin Institute of Technology, Shenzhen 518055, China

²School of Astronomy and Space Science, Nanjing University, Nanjing 210023, China

³CAS Key Laboratory of Geospace Environment, School of Earth and Space Sciences, University of Science and Technology of China, Hefei, Anhui 230026, China

⁴School of Atmospheric Sciences, Sun Yat-Sen University, Zhuhai 519000, China

⁵State Key Laboratory for Space Weather, Center for Space Science and Applied Research, Chinese Academy of Sciences, Beijing 100190, China

ABSTRACT

Magnetic flux ropes (MFRs) constitute the core structure of coronal mass ejections (CMEs), but hot debates remain on whether the MFR forms before or during solar eruptions. Furthermore, how flare reconnection shapes the erupting MFR is still elusive in three dimensions. Here we studied a new MHD simulation of CME initiation by tether-cutting magnetic reconnection in a single magnetic arcade. The simulation follows the whole life, including the birth and subsequent evolution, of an MFR during eruption. In the early phase, the MFR is partially separated from its ambient field by a magnetic quasi-separatrix layer (QSL) that has a double-J shaped footprint on the bottom surface. With the ongoing of the reconnection, the arms of the two J-shaped footprints continually separate from each other, and the hooks of the J shaped footprints expand and eventually become closed almost at the eruption peak time, and thereafter the MFR is fully separated from the un-reconnected field by the QSL. We further studied the evolution of the toroidal flux in the MFR and compared it with that of the reconnected flux. Our simulation reproduced an evolution pattern of increase-to-decrease of the toroidal flux, which is reported recently in observations of variations in flare ribbons and transient coronal dimming. The increase of toroidal flux is owing to the flare reconnection in the early phase that transforms the sheared arcade to twisted field lines, while its decrease is a result of reconnection between field lines in the interior of the MFR in the later phase.

Keywords: Magnetic fields; Magnetohydrodynamics (MHD); Methods: numerical; Sun: corona; Sun: flares

1. INTRODUCTION

Solar eruptions are spectacular manifestation of explosive release of magnetic energy in the Sun's atmosphere, i.e., the solar corona, and therefore, unveiling the relevant magnetic field structures and their evolution holds a central position in the study of solar eruptions. Magnetic flux rope (MFR), a bundle of twisted magnetic field lines winding around a common axis with the same sign, is believed to be a fundamental structure in solar eruptions (Cheng et al. 2017; Duan et al. 2019; Liu 2020), especially in those which successfully produce coronal mass ejections (CMEs). By reconstruction of the cross section of ICME (i.e., CMEs that evolves into the inter-planetary space) from the in-situ data obtained by satellites passing through the ICME, it has been well established that typical ICMEs have structure of highly twisted MFR (e.g., Wang et al. 2016; Hu 2017).

Although there is little doubt that MFR constitutes the core structure of CMEs, whether MFR exists in the solar corona before CME initiation is still in intense debates (Chen 2011; Patsourakos et al. 2020). Currently, there are two different opinions; one is that MFR does not exist before solar eruption, and it is the latter that creates MFR through magnetic reconnection; the other is that MFR should exist prior to eruption and it is the ideal magnetohydrodynamic (MHD) instability of the MFR that initiates the eruption. The typical scenarios for the first opinion include the runaway tether-cutting reconnection model (Moore & Labonte 1980; Moore & Roumeliotis 1992; Moore et al. 2001) and the magnetic breakout model (Antiochos et al. 1999; Aulanier et al. 2000; Lynch et al. 2008; Wyper et al. 2017). In these models, the coronal magnetic field before eruption is strongly sheared and eruption is triggered by magnetic reconnection, internally within the sheared arcade (i.e., tether-cutting), or above it (i.e., breakout), while MFR is built up during the eruption through reconnection which transforms the sheared arcade into the rope. For the models assuming the pre-existence

*Corresponding author: chaowei@hit.edu.cn

of MFR, such as the catastrophe model (Forbes & Isenberg 1991; Lin et al. 2001), the torus instability and kink instability models (Kliem & Török 2006; Török & Kliem 2005; Fan & Gibson 2007; Aulanier et al. 2010; Amari et al. 2018), an MFR is proposed to either emerge from below the photosphere (i.e., in the convective zone, where the turbulent convection can create thin, twisted magnetic tubes, Fan 2001; Cheung & Isobe 2014), or forms slowly by reconnection in the lower atmosphere (Green et al. 2011) through the so-called flux cancellation process (van Ballegooijen & Martens 1989). Observations seem to indicate that both opinions are possible. For example, on one hand, Song et al. (2014) presented a good observation that an MFR can be formed during a CME. On the other hand, an MFR characterized by a hot sigmoid structure may pre-exist before eruption, as manifested by precursor oscillation (Zhou et al. 2016) or precursor external magnetic reconnection between the top of the MFR and ambient magnetic field (Zhou et al. 2019).

Regardless of which model is relevant to the real case in the corona, it is commonly agreed that flare reconnection (i.e., the main reconnection that occurs below the erupting MFR) can shape substantially the on-the-fly MFR. In the purely two-dimensional (2D) standard flare model, a plasmoid (corresponding to the cross section of MFR in 3D) rises from the top of the flare current sheet, and reconnection in the current sheet continuously adds poloidal flux to the MFR, which thus grows and expands during the eruption. As a result, the observed double flare ribbons, which indicate the locations of the reconnecting field-line footpoints in the opposite magnetic polarities, are continuously separated with each other. However, in a fully 3D case, it is not that straightforward how the reconnection shapes the MFR. Numerical simulations of the simplest magnetic configuration (i.e., a bipolar magnetic field), aided with accurate analysis of magnetic topology evolution, have been developed to study how an MFR evolves with reconnection during eruption (Aulanier et al. 2010, 2012), and the findings are becoming known as the standard flare model in 3D (Aulanier et al. 2012; Janvier et al. 2013, 2014), although it is still an over-simplified version of the realistic cases as demonstrated in recent data-constrained and data-driven simulations (e.g., Jiang et al. 2018; Jiang et al. 2018; Zhong et al. 2021).

In the standard 3D model, the erupting MFR is separated from the ambient field by a quasi-separatrix layer (QSL Demoulin et al. 1996), and in more details, this QSL intersects with itself below the MFR, forming a hyperbolic flux tube (HFT, Titov et al. 2002), and the flare reconnection occurs mainly in the HFT. The footprints of this QSL at the bottom surface, i.e., the photosphere, forms two thin strips of J shape on each side of the main polarity inversion line (PIL), and the legs of the MFR are anchored within the hooked parts of the J-shaped strips. Thus, the observed flare ribbons usually exhibit double-J pattern, and the transient coronal holes (Kahler & Hudson 2001), i.e., post-eruptive twin

coronal dimmings, are naturally suggested to map the feet of erupting MFRs, along which mass leakage into interplanetary space could take place (Webb et al. 2000; Qiu et al. 2007; Xing et al. 2020), and the boundaries of such twin coronal dimmings are outlined by the hooks of flare ribbons. With the ongoing of reconnection, the arms of the double-J ribbons separate, and their hooks gradually extend outwards. In such process, the flare reconnection, which occurs between the pre-reconnection sheared arcade (as shown in the classic cartoon of tether-cutting model, i.e., Figure 1 of Moore et al. 2001), should increase the toroidal (axial) flux by increasing the number of field lines within the MFR.

However, such a ‘standard’ type of flare reconnection in 3D still cannot explain fully the observations of ‘standard’ two-ribbon flares. A well-known, unexplained fact is that the feet of the erupting flux rope, as manifested by twin coronal dimmings and also by the hook ends of double-J flare ribbons, are found to be drifting progressively away from the main PIL during eruption (Kahler & Hudson 2001), even though the photosphere can be regarded as motionless during the short time scale of eruption. To this end, Aulanier & Dudík (2019) analyzed in more details the reconnection process in their simulation of flux rope eruption and showed that the flare reconnection actually occurs in three different types of events according to their different effect in building up the flux rope. The first one is named as *aa-rf reconnection*, which is the standard 3D flare reconnection that occurs between two arcades and results in a long field line joining the flux rope and a short one as a flare loop. The second one is the so-called *rr-rf reconnection*, which occurs within the flux rope by reconnecting two flux-rope field lines with each other and generates a new multi-turn flux-rope field line and a flare loop. The third one is *ar-rf reconnection*, in which an inclined arcade reconnects with the leg of a flux-rope field line, and it generates new flux-rope field line rooted far away from the PIL and a flare loop. Thus, it is the *ar-rf reconnection* that actually leads to gradual drifting of the MFR footprints.

Observations show even more features not explained (or not mentioned) in the ‘advanced’ standard model of Aulanier & Dudík (2019). For instance, using high-resolution observations, Wang et al. (2017) found two closed-ring-shaped flare ribbons in the case of a buildup of highly twisted MFRs with the development of a flare reconnection. During the separation of the main flare ribbons, the flare rings expand significantly, starting from almost point-like brightening. Note that such closed circular shape flare ribbons have different nature from those formed by null-point topology which also produce circular ribbon due to reconnection in the null’s spine-fan separatrix (Jiang et al. 2018). It is predicted by theoretical models (Demoulin et al. 1996) that if the MFR grows to sufficiently twisted, the hooks of the double-J shaped footprints of the QSL can indeed close onto themselves, becoming two closed rings, although this is not reproduced by the numerical model of (Aulanier et al. 2010), possibly because

their simulation run is stopped before the MFR grows to such a high degree of twist.

Very recently, a few papers reported that there is a systematic decrease of the toroidal flux of erupting MFR after its fast increase (e.g., Wang et al. 2017; Chen et al. 2019; Xing et al. 2020). In particular, Xing et al. (2020) developed a practical method for estimation of the toroidal flux of MFR during eruption by combining twin coronal dimmings and the hooks of flare ribbons. They found that the toroidal flux of the CME flux rope for all four studied events shows a two-phase evolution: a rapid increasing phase followed by a decreasing phase, and moreover, the evolution is well synchronous in time with that of the flare soft X-ray flux. The increase of MFR’s toroidal flux can be easily understood by the *aa-rf reconnection* while the subsequent decrease remains unclear. Although Xing et al. (2020) invoked the *rr-rf reconnection* as the mechanism responsible for such decrease, it is still unknown whether the increase-to-decrease evolution of toroidal flux can self-consistently be reproduced in any MHD simulation.

This series of papers are devoted to a comprehensive analysis of a new MHD simulation of eruption (Jiang et al. 2021), focusing on the formation of MFR during eruption. That simulation demonstrated in fully 3D that solar eruption can be initiated from a single magnetic arcade without the formation of MFR before the triggering of eruption. This is different from the aforementioned simulations (Aulanier et al. 2010; Aulanier & Dudík 2019), in which the eruption is initiated by torus instability (which is a kind of ideal MHD instability, Kliem & Török 2006) of an MFR formed well before the eruption. With the new MHD simulation, one can follow whole life, i.e., the birth and subsequent evolution, of an MFR during the eruption. As the first paper of this series, here we show, for the first time, that both the closing of the hook ends of the QSLs at the MFR’s feet and the increase-to-decrease evolution of the toroidal magnetic flux can be self-consistently reproduced by the simulation, suggesting that they are genuine features of erupting MFRs. We further quantified the evolution of reconnection flux during the eruption, and found that the evolution of QSLs is rather complex within the MFR. In the second article of this series, we will illustrate the 3D configuration of the different types of magnetic reconnection in building up the MFR and disclose why the QSLs evolve in such a complex way, following the pioneering work by Aulanier & Dudík (2019).

2. MHD SIMULATION AND ANALYSIS METHOD

Recently, Jiang et al. (2021) performed an ultra-high accuracy, fully 3D MHD simulation and demonstrated that solar eruptions can be initiated in a single sheared arcade with no additional special topology. Their simulation shows that, “through photospheric shearing motion alone, an electric current sheet forms in the highly sheared core field of the magnetic arcade during its quasi-static evolution. Once mag-

netic reconnection sets in, the whole arcade is expelled impulsively, forming a fast-expanding twisted flux rope with a highly turbulent reconnecting region underneath”. They further found that the high-speed reconnection jet plays the key role in driving the eruption. The simplicity and efficacy of this scenario, in the theoretical point of view, argue strongly for its fundamental importance in the initiation of solar eruptions. Since the model do not need a pre-existing MFR, the MFR itself comes into being *after* the eruption initiation.

Here we focus on the formation and evolution of MFR during the eruption by using a simulation run like the one in Jiang et al. (2021), but with a lower resolution than the original ones. Such simulation solves the full set of MHD equations and starts from a bipolar potential magnetic field and a hydrostatic plasma stratified by solar gravity with typical coronal temperature. Then shearing flows along the PIL, which are implemented by rotating the two magnetic polarities at the photosphere in the same count-clockwise direction, are applied on the bottom boundary to energize the coronal field until an eruption is triggered, and after then the surface flow is stopped. The whole computational box extends as $(-32, -32, 0) < (x, y, z) < (32, 32, 64)$ with length unit of 11.5 Mm. We solve a full MHD equation with both solar gravity and plasma pressure included, but with the energy equation simplified as an isothermal process. The time unit of the model is $\tau = 105$ s, and the shearing motion is applied by approximately 120τ before the onset of the eruption, during which a current sheet is gradually built up. Since no explicit resistivity is used in the MHD model, magnetic reconnection is triggered when the current sheet is sufficiently thin such that its width is close to the grid resolution. For more details of the simulation settings, the readers are referred to Jiang et al. (2021). In that paper, the simulation is managed to be of very high resolutions with Lundquist number achieving $\sim 10^5$ for a length unit. Therefore, the secondary tearing instability (or plasmoid instability) is triggered in the current sheet and the magnetic topology becomes extremely complicated in small scales along with formation of the large-scale MFR. Such a complexity substantially complicates our analysis of the large-scale magnetic topology evolution associated with the erupting MFR, thus in this paper we used a lower-resolution run (corresponding to a Lundquist number of $\sim 10^3$). In the lower-resolution run, the basic evolution of the MFR during the eruption is not changed as compared to the high-resolution run, except that the small-scale structure will not arise, and thus the QSLs are computed in a cleaner pattern. Moreover, with the lower resolution, we can run the simulation longer and thus follow a longer evolution of MFR.

To help revealing the variation of the magnetic topology, we study the distribution and evolution of two parameters, the magnetic squashing degree and the magnetic twist number, which are commonly used for the study of 3D magnetic fields and their dynamics (Aulanier et al. 2012; Janvier et al. 2013; Inoue et al. 2013; Savcheva et al. 2016; Liu et al. 2016;

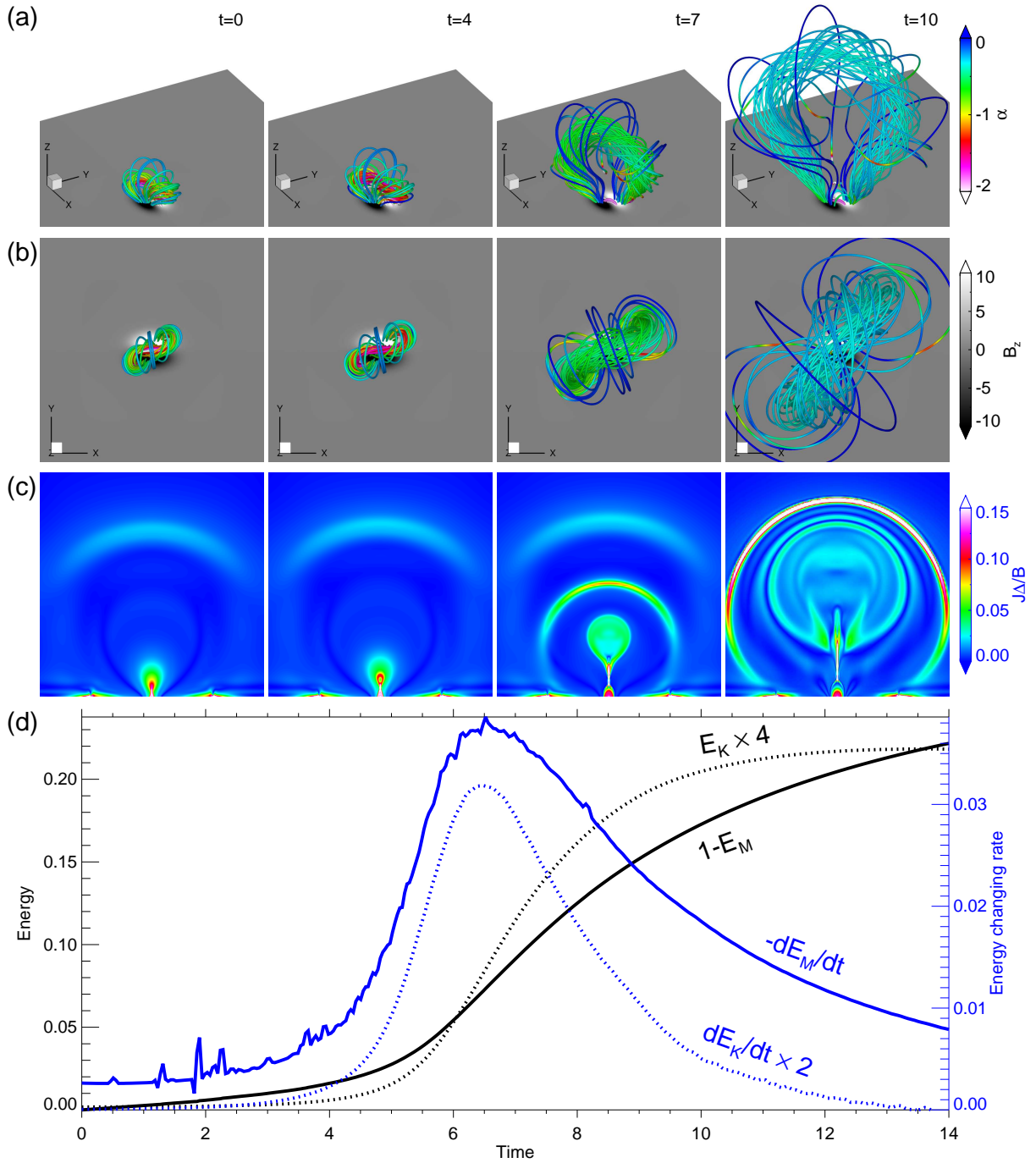


Figure 1. Structural evolution of the eruption. (a) 3D prospective view of magnetic field lines colored by the force-free factor. Here the field lines are traced at fixed footpoints on the bottom surface, and they represent the core structure of the pre-eruption field. (b) Top view of the structure shown in (a). (c) Evolution of the dimensionless current density $J\Delta/B$ on the central cross section (i.e., the $x=0$ slice). (d) Evolution of magnetic and kinetic energies and their temporal changing rate. The energies are all normalized by the magnetic energy at $t=0$ and the unit of time is 105 s. Also see Supplementary Movie 1 for a high-cadence evolution of the eruption process.

Duan et al. 2019). The magnetic squashing degree Q quantifies the gradient of magnetic field-line mapping with respect to their footpoints, and it is helpful for searching QSLs (and true separatrixes) of magnetic fields (Titov et al. 2002), which can have extremely large values of Q (e.g., $\geq 10^5$) and are preferential sites of magnetic reconnection. By locating the QSLs from the high values of Q we can see how the magnetic topology is evolved by the magnetic reconnection. Specifically, for a field line starting at one footpoint (x, y) and ending at the other footpoint (X, Y) where X and Y are both functions of x and y , the squashing degree Q associated with this field line is given by (Titov et al. 2002)

$$Q = \frac{a^2 + b^2 + c^2 + d^2}{|ad - bc|} \quad (1)$$

where

$$a = \frac{\partial X}{\partial x}, \quad b = \frac{\partial X}{\partial y}, \quad c = \frac{\partial Y}{\partial x}, \quad d = \frac{\partial Y}{\partial y}. \quad (2)$$

The magnetic twist number T_w (Berger & Prior 2006) is defined for a given (closed) field line by taking integration of $T_w = \int_L \mathbf{J} \cdot \mathbf{B} / B^2 dl / (4\pi)$ along the length L of the field line between two conjugated footpoints on the photosphere. Note that T_w is not identical to the classic winding number of field lines about a common axis, but an approximation of the number of turns that two infinitesimally close field lines wind about each other (Liu et al. 2016).

3. RESULTS

3.1. Overview of the eruption

Figures 1 (and Supplementary Movie 1) shows the magnetic field lines, current density, and energies evolution from slightly before the eruption onset to a time well after the eruption peak time (that is, the peak time of energy conversion rate, which is $t = 6.5$). As can be seen, our simulation demonstrates a typical coronal eruption leading to a CME, as seen in observations as well as many previous numerical simulations with different scenarios (Linker et al. 2003; Amari et al. 2003; Török et al. 2018). The core magnetic field changes from the pre-eruptive sheared arcades to a inverse S-shaped MFR structure that subsequently exhibits a huge growth in size. From the top view, the MFR axis shows a significant anti-clockwise rotation during the eruption. Figure 1c shows a dimensionless current density, defined as $J\Delta/B$ (where J is the current density, Δ is the grid resolution and B is the magnetic field strength), on the central cross section, i.e., the $x = 0$ slice of the 3D volume. One can see a picture of the 2D standard flare model: a plasmoid rises and leaves behind a cusp structure corresponding to the edge of post-flare loop, and connecting them is a long CS in which magnetic reconnection occurs continuously. This reconnection results in high-speed bi-directional (up and down) plasma jets due to the “slingshot” effect, and the upward jet flow continuously pushes outward the newly

reconnected magnetic flux. Eventually, it produces a CME and drives an arc-shaped fast magnetosonic shock enclosing the erupting structure.

3.2. Evolution of Magnetic Squashing Factor and Twist Number

To analyze the evolution of magnetic topology, in particular the formation of MFR, during the simulated eruption, we calculate the magnetic squashing factor Q and magnetic twist number T_w at the bottom surface and at a vertical central cross section of the 3D volume. The results are shown in Figure 2 for a few snapshots and Supplementary Movie 2 for the whole evolution. At the bottom surface, initially there are two thin strips of high Q , i.e., QSLs (or more precisely, the footprints of QSLs), forming two J shapes on either side of the PIL. With onset of the eruption, the two J-shaped QSLs on the bottom surface begin to evolve rapidly (see Figure 2a and the high-cadence evolution in Supplementary Movie 2). In Figure 3a and b, we show the field lines traced from the bottom QSLs at two different times, and the 3D structure of the reconnection current sheet by an iso-surface of extremely strong current density. As can be seen, all the field lines pass through the reconnection current sheet, which demonstrates clearly that the field lines in the QSLs are undergoing reconnection. Consequently, the motion of the bottom QSLs corresponds to the apparent motion of footpoints of the field lines that were undergoing reconnection. Furthermore, from Figure 3, one can see that in the early phase the reconnection is a fully 3D manner with a strong guide field component (i.e., B_x) because joining in the reconnection is mainly the strongly sheared, low-lying flux. While in the later phase, as the sheared flux has been reconnected, the reconnection transfers into a quasi-2D manner, which consumes mainly the large-scale, overlying flux that is barely sheared.

On the central cross section (Figure 2c), the QSLs intersect with each other, developing into an X shape, i.e., an HFT (Titov et al. 2002), and the intersection X point is essentially the reconnection site (in analogy to the null point in a 2D X-shaped reconnection configuration). As the eruption proceeds, more and more magnetic fluxes reconnect, and consequently, the two J-shaped QSLs on the bottom surface continuously separate with each other (see also Figure 3c, in which the separation speed is estimated). In the end of the simulation, they have swept to the center of each magnetic polarity (which is analogous to the umbra of sunspot). Meanwhile, the X point of the HFT rises upward progressively (see also Figure 3d, in which the rising speed is estimated) with the cusp region expanding below. Such two QSLs with their separation should be manifested as two separating flare ribbons in observations (Savcheva et al. 2016; Jiang et al. 2018), while the rise of the X point corresponds to the apparent rising of the apex of post-flare arcades.

Figure 2b and d present the T_w distribution on the bottom surface and the central cross section, respectively. Starting

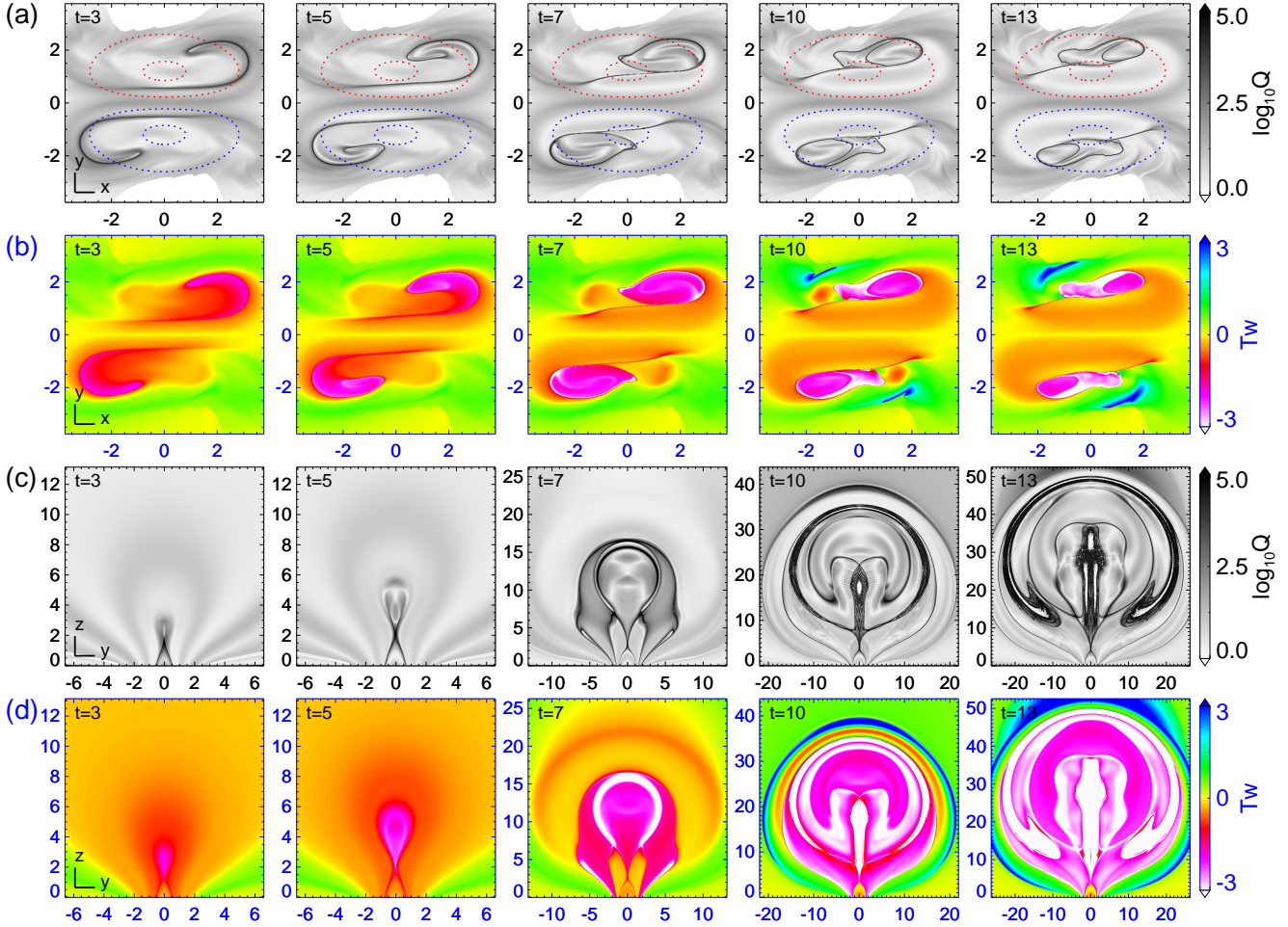


Figure 2. Magnetic topology evolution and formation of MFR during the eruption. (a) Magnetic squashing degree Q on the bottom surface. The dashed lines are contours of $B_z = -5, -10$ (blue) and $5, 10$ (red). (b) Magnetic twist number T_w on the bottom surface. (c) and (d) show the two parameters Q and T_w on the central vertical cross section (i.e., $x = 0$ plane). Also see Supplementary Movie 2 for a high-cadence evolution.

from the hooks of the J-shaped QSLs, magnetic flux with high twist (as denoted by large absolute values of T_w) begins to form owing to the tether-cutting reconnection, which creates long field lines connecting the far ends of the two pre-reconnection sheared arcades. With the twisted flux accumulated through the continuation of reconnection, the areas occupied by the footpoints of the highly twisted field lines at the hooks expand. Consequently, the hook of each J-shaped QSL continuously extends inward until its end reaches the arm, forming a closed curve encircling the highly twisted flux (see the QSL at $t = 7$). Such a transition of QSLs reproduces the evolution of flare ribbons that gradually forms close rings at their ends (Wang et al. 2017). With this, the MFR is *fully* separated with its surroundings by the QSLs. Consistently, as can be seen in the vertical cross section at $t = 7$, the QSL form a closed tear-drop shape connecting the HFT, within which the twisted flux of the MFR has twist number T_w mostly below -2 .

The evolution speed of the QSLs is related to the rate of reconnection. As shown in Figure 3c, at the beginning of

the eruption, the distance of the two QSLs is about 10 Mm, and it reaches ~ 30 Mm at the end of the simulation. The separation speed first increases and then decreases, with its largest value of about 18 km s^{-1} at the time of around $t = 6.5$, which is also the time the plasma acceleration reaches its maximum (see Figure 1). Meanwhile, the rising speed of the X point, i.e., the apex of the cusp structure reaches a maximum of about 40 km s^{-1} . Our simulated flare-ribbon distances, their separation speed as well as the rising speed of the cusp are all comparable to typical observed ones (Wang et al. 2003; Qiu et al. 2009; Hinterreiter et al. 2018; Yan et al. 2018).

Nearly at the same time when the hook ends of the J-shaped QSLs close, there is even a new QSL forms within the closed QSLs (see $t = 10$ and $t = 13$ in Figure 2a). In the positive polarity, for example, this new QSL is bifurcated from the hook end and moves to the right. As a result, the region bounded by the closed QSL, i.e., the foot of the MFR, is divided into two regions separated by the newly formed QSL, and the region after swept by the new QSL shows even

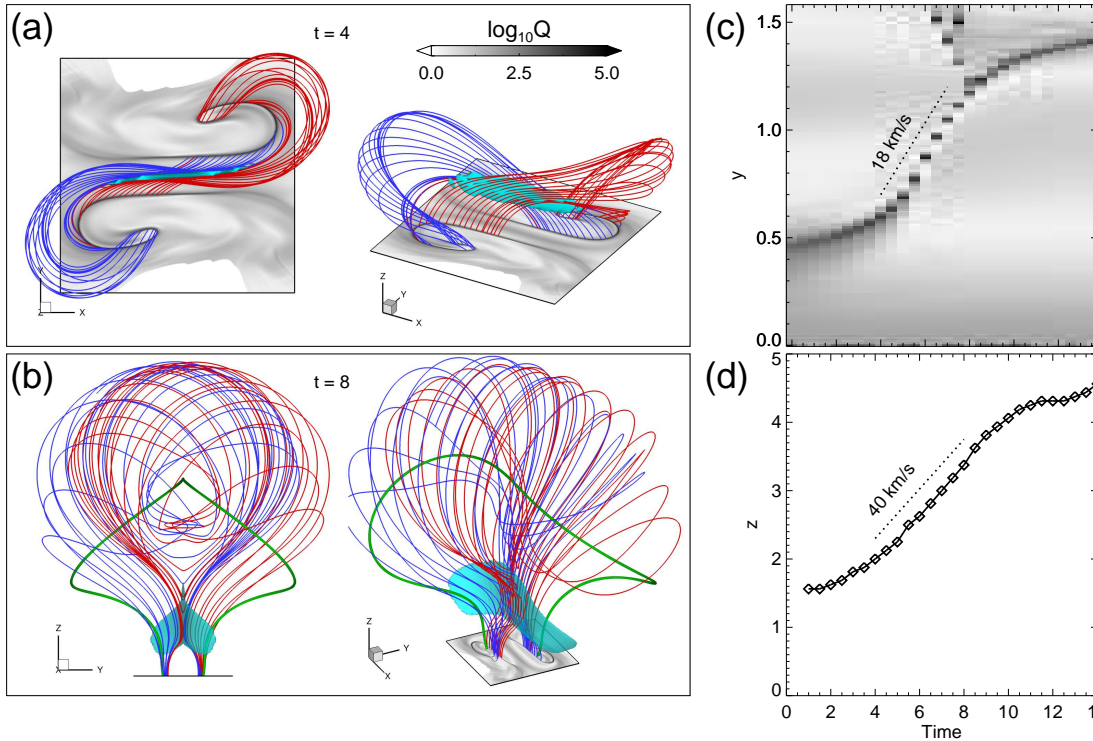


Figure 3. Details of reconnection. (a) Structure of the reconnecting field lines at $t = 4$. The field lines are colored in red and blue. The cyan object is the iso-surface of $J\Delta/B = 0.2$, i.e., the reconnection CS. The magnetic field lines are traced from the QSLs shown on the bottom surface, and as can be seen, they all contact the CS as these field lines are undergoing reconnection. (b) Sample of reconnecting field lines at $t = 8$. The thick green lines represent the axis of the newly formed MFR. Note that the actual sizes of the bottom surfaces shown in (a) and (b) are identical. (c) A stacked time sequence of the bottom Q map in y -direction and centred at $x = 0$, which shows the separation motion of the two J-shaped QSLs shown in Figure 2(a). The sloped, dashed line denotes the largest separation speed. (d) Time evolution of the height of X point of the hyperbolic flux tube, i.e., the apex of the cusp structure, shown in Figure 2(c). The sloped, dashed line denotes the largest rising speed.

stronger magnetic twist than before. This indicates that there must be internal reconnection between different field lines of the MFR. Another noticeable change is the decrease of the area in the closed QSLs, i.e., the feet of the MFR, which is quantified below.

3.3. Evolution of MFR's Toroidal Flux

The toroidal flux of the MFR, i.e., the content of the rope's flux that connects the bottom surface, can be quantified by using the distributions of twist number T_w and squashing factor Q at the bottom surface. Before the full closing of the hook ends of the QSLs, the feet of the MFR are characterized by the high T_w areas, while after the closing of the hooked QSLs, they can be identified more accurately by the area within the closed QSLs, but the T_w is still a good indicator since the QSL-enclosed region has a distinctly strong twist number (compare T_w and Q in Figure 2). We thus directly use the distribution of T_w to locate the MFR's feet in the whole evolution. However, it should be noted that the T_w provides only an approximation of the classic definition of the winding number around a common axis, and that there is no consensus on the definition of MFR based on either the winding number or the twist number T_w , although it is

generally agreed that the winding of field lines in an MFR should be at least one turn. Therefore, we use two different thresholds for T_w to locate the MFR, and two values of the toroidal flux of the MFR are calculated by summing the magnetic flux with T_w exceeding the two thresholds, respectively. One is $T_w \leq -1$, which is also used by Duan et al. (2019) for searching MFRs in coronal field extrapolations, and the other is $T_w \leq -1.5$, which is properly chosen such that the MFR can be clearly differentiated from the background flux that has moderate twist number of $T_w \sim -1$ but without reconnection during the eruption (thus remains non-flux-rope field lines during the eruption). We also compute the areas of the MFR foot using the two thresholds, as well as the average twist number of the toroidal flux. The results are present in Figure 4a and b, which clearly show that the toroidal flux (as computed by either thresholds) first increases, reaching its peak value fast, and then decrease slowly. Such an evolution pattern also applies to that of the MFR foot area. This increase-to-decrease pattern of toroidal flux reproduces the observed variations of magnetic flux in erupting MFR's foot as identified by flare ribbons and transient coronal dimming (Xing et al. 2020). On the other hand, the mean twist number shows a systematic increase to a value

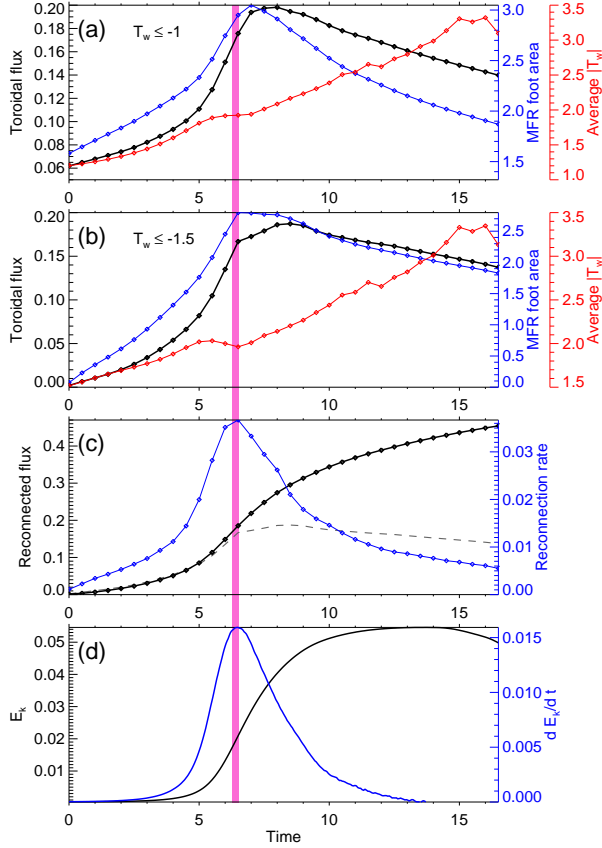


Figure 4. Temporal evolution of different parameters in the eruption. (a) Toroidal flux (black line), foot area (blue line) and average twist number (red line) of the MFR as calculated with $T_w \leq -1$. They are defined as, respectively, $\int_S B_z ds$, area of S and $\int_S B_z T_w ds / \int_S B_z ds$, in which S is the region of $T_w \leq -1$ at the bottom surface. (b) Same as (a) but with $T_w \leq -1.5$. (c) Magnetic reconnected flux and its increasing rate. The dashed line shows the toroidal flux with $T_w \leq -1.5$. (d) Kinetic energy and its changing rate. The pink vertical bar denotes the peak time of the increasing rate of kinetic energy.

close to 3.5 at the end of simulation.

3.4. Evolution of Reconnection Flux

We further quantify how much of the magnetic flux is reconnected during the eruption. In principle, the total reconnected flux is simply the flux (by a factor of two) that is swept by the QSLs at the bottom surface in magnetic polarities of the same sign. This is analogous to counting the photospheric magnetic flux swept by flare ribbons to measure reconnection rate from direct observations (Qiu et al. 2002; Wang et al. 2003). However, this requires a very high time cadence of simulated data to capture the fast motion of the QSLs, such that the combination of all the QSLs at different times can seamlessly forms the whole area that experiences reconnection. Furthermore, the geometry of QSLs is rather complex, and it is not straightforward to compute the areas swept by the QSLs. For instance, in Figure 5a, the QSLs at two consecutive times ($t = 6$ and 6.5) are over-plotted. As can be

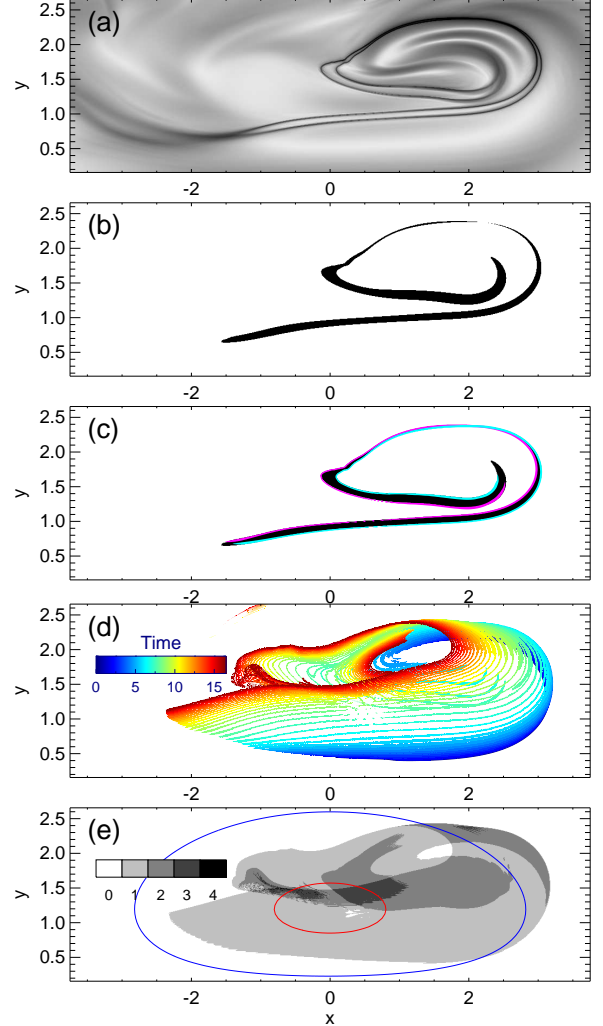


Figure 5. Areas swept by the QSLs at the bottom surface. (a) A overlaid image of Q at two consecutive times $t = 8$ and 8.5 . (b) The reconnected region (shown in black) as calculated by using the slipping of the field line footpoints. (c) Same as (b) and overlaid with the QSLs at $t = 8$ (colored in cyan) and $t = 8.5$ (colored in pink). (d) Overlaid plot of the QSLs at all the different times from $t = 0$ to 16.5 . The QSLs at different times are color coded by time. (e) All the regions swept by the QSL. Note that some regions are swept by the QSL with more than one time, and the swept times are denoted by gray color. Two contours of B_z , 10 (red) and 5 (blue), are overlaid for showing the location of the magnetic polarity.

seen, there are clearly a margin between them, and this margin area is exactly the region swept by the QSL in the time increment (i.e., from $t = 6$ to 6.5). It is not easy to calculate the flux in this bounded area owing to its very irregular shape.

Thus, we proposed an alternative way to calculate the reconnected flux by taking advantage of the fast-slipping motion of the footpoints of the reconnected field lines. In our simulation the bottom surface is fixed without any motion, thus for any field line without reconnection, it will be perfectly frozen with the plasma, and its two footpoints will not

change with time. So, if tracing from a fixed footpoint of a field line to the other end, the conjugate footpoint will also be a fixed point at different times. If the field line undergoes reconnection, the conjugate footpoint will slip to a different location in the time step, and thus by the displacement one can easily find whether the field line reconnects or not during the time step. By this approach, the region between the two QSLs at the two consecutive times is clearly enhanced, as shown in Figure 5b and c, and then we can calculate the reconnected flux in the time step. In Figure 5d all the QSLs at different times (in one polarity) are overlaid, and in Figure 5e all the regions swept by the moving QSL are shown. We note that a large portion of the polarity is swept and therefore reconnects during the eruption, and an evident drift of the MFR foot can be seen. Interestingly, there are some regions that are swept by the QSL with more than one time, some even reaching 4 times, suggesting a rather complex internal reconnection in the erupting MFR.

The reconnection flux and its changing rate are shown in Figure 4c. The total reconnected flux increases monotonically, attaining nearly half of AR's total flux content at the end of the simulation. The reconnection rate, i.e., the increasing rate of the reconnected flux, shows an evolution pattern (i.e., fast increase and then slow decrease) like the changing rate of the kinetic and magnetic energies (see also Figure 1), and all of them reach the peak at the same time. Such temporal correlation between reconnection rate (or flare emission) and CME acceleration has been well revealed in observation studies (Zhang et al. 2001; Qiu et al. 2004), stressing the central role and fundamental importance of magnetic reconnection in producing flare and CME (Zhu et al. 2020).

It is interesting to compare evolution of the MFR's toroidal flux and that of the reconnected flux. In Figure 4c, the dashed line shows the toroidal flux as present in Figure 4b. In the early stage, i.e., before the reconnection rate reaches its peak, the reconnected flux almost equals to the toroidal flux, meaning that the reconnection builds up the MFR by transferring the same amount of sheared arcade flux into the same amount of flux in the rope. However, after the peak time, although the reconnected flux continues to increase, the toroidal flux in the rope decreases, and this suggesting that there must be reconnection within the MFR, by the so-called *rr-rf* reconnection (Aulanier & Dudík 2019). We note that, interestingly, the peak time of reconnection rate (at $t = 6.5$) also coincides with the time of the closing of the QSLs, and immediately afterward, the toroidal flux also reaches its maximum.

4. SUMMARY

In this paper, we have studied the magnetic evolution of an MFR formed during the eruption in an MHD simulation. The MFR is generated absolutely by tether-cutting recon-

nection of the pre-eruption, strongly sheared arcade. In the early phase, the MFR is partially separated from its ambient field by a QSL that has a double-J shaped footprint on the bottom surface. With the ongoing of the reconnection, the arms (i.e., the straight parts) of the two J-shaped footprints continually separate from each other, which eventually pass through the centers of each polarity. Meanwhile, the hooks of the J shaped footprints expand and eventually become closed almost at the eruption peak time, and thereafter the MFR is fully separated with the un-reconnected field by a QSL. The reconnection substantially shapes the MFR by first increasing quickly and then decreasing gradually its total toroidal flux, which explains a recent observation of magnetic flux variation in erupting MFR's foot. In the whole eruption, nearly half of the AR's flux is reconnected, and the reconnection rate, as measured by the increasing rate of the reconnection flux, synchronizes well with the energy conversion rate (i.e., magnetic energy releasing rate and the kinetic energy increasing rate). In the early stage, i.e., before the reconnection rate reaches its peak, the reconnected flux almost equals to the toroidal flux in the MFR, whereas after the peak time the toroidal flux in the MFR decreases despite that the reconnected flux continues to increase. The increase of toroidal flux is owing to the flare reconnection in the early phase that transforms the sheared arcade to twisted field lines, while its decrease should be a result of reconnection between field lines in the interior of the MFR in the later phase, as first disclosed in (Aulanier & Dudík 2019).

Our simulation shows that the QSLs associated with the MFR in the later phase become more complex than expected, since there are new QSLs formed within the MFR, while the flux associated with these new QSLs becomes extremely highly twisted. This is due to a fast expansion of the MFR as well as its complex 3D nature, and thus at certain locations field lines reconnect with others in the MFR or themselves. Such reconnection may happen multiple times for field lines rooted at the same locations, even making some of field lines self-closed in the corona, which might be an important way for a CME flux to be totally detached from the Sun. The details of such complexity and the involved reconnection, and whether such complexity is hinted in observation, are to be elaborated in future works.

This work is jointly supported by National Natural Science Foundation of China (NSFC 4217040250, 41822404, 41731067) and Shenzhen Technology Project JCYJ20180306171748011. The computational work was carried out on TianHe-1(A), National Supercomputer Center in Tianjin, China.

REFERENCES

- Antiochos, S. K., DeVore, C. R., & Klimchuk, J. A. 1999, *ApJ*, 510, 485
- Aulanier, G., DeLuca, E. E., Antiochos, S. K., McMullen, R. A., & Golub, L. 2000, *ApJ*, 540, 1126
- Aulanier, G. & Dudík, J. 2019, *Astronomy & Astrophysics*, 621, A72
- Aulanier, G., Janvier, M., & Schmieder, B. 2012, *A&A*, 543, A110
- Aulanier, G., Török, T., Démoulin, P., & DeLuca, E. E. 2010, *ApJ*, 708, 314
- Berger, M. A. & Prior, C. 2006, *Journal of Physics A Mathematical General*, 39, 8321
- Chen, H., Yang, J., Ji, K., & Duan, Y. 2019, *The Astrophysical Journal*, 887, 118
- Chen, P. F. 2011, *Living Reviews in Solar Physics*, 8, 1
- Cheng, X., Guo, Y., & Ding, M. 2017, *Science China Earth Sciences*, 60, 1383
- Cheung, M. C. M. & Isobe, H. 2014, *Living Reviews in Solar Physics*, 11
- Démoulin, P., Henoux, J. C., Priest, E. R., & Mandrini, C. H. 1996, *A&A*, 308, 643
- Duan, A., Jiang, C., He, W., Feng, X., Zou, P., & Cui, J. 2019, *The Astrophysical Journal*, 884, 73
- Fan, Y. 2001, *ApJL*, 554, L111
- Fan, Y. & Gibson, S. E. 2007, *ApJ*, 668, 1232
- Forbes, T. G. & Isenberg, P. A. 1991, *ApJ*, 373, 294
- Green, L. M., Kliem, B., & Wallace, A. J. 2011, *Astronomy & Astrophysics*, 526, A2
- Hinterreiter, J., Veronig, A. M., Thalmann, J. K., Tschernitz, J., & Pötzi, W. 2018, *SoPh*, 293, 38
- Hu, Q. 2017, *Science China Earth Sciences*, 60, 1466
- Inoue, S., Hayashi, K., Shiotani, D., Magara, T., & Choe, G. S. 2013, *ApJ*, 770, 79
- Janvier, M., Aulanier, G., Bommier, V., Schmieder, B., Démoulin, P., & Pariat, E. 2014, *The Astrophysical Journal*, 788, 60
- Janvier, M., Aulanier, G., Pariat, E., & Démoulin, P. 2013, *Astronomy & Astrophysics*, 555, A77
- Jiang, C., Feng, X., & Hu, Q. 2018, *The Astrophysical Journal*, 866, 96
- Jiang, C., Feng, X., Liu, R., Yan, X., Hu, Q., Moore, R. L., Duan, A., Cui, J., Zuo, P., Wang, Y., & Wei, F. 2021, *Nature Astronomy*, 10.1038/s41550-021-01414-z
- Jiang, C., Zou, P., Feng, X., Hu, Q., Liu, R., Vemareddy, P., Duan, A., Zuo, P., Wang, Y., & Wei, F. 2018, *ApJ*, 869, 13
- Kahler, S. W. & Hudson, H. S. 2001, *J. Geophys. Res.*, 106, 29239
- Kliem, B. & Török, T. 2006, *Physical Review Letters*, 96, 255002
- Lin, J., Forbes, T. G., & Isenberg, P. A. 2001, *J. Geophys. Res.*, 106, 25053
- Linker, J. A., Mikić, Z., Lionello, R., Riley, P., Amari, T., & Odstrčil, D. 2003, *Physics of Plasmas*, 10, 1971
- Liu, R. 2020, *Research in Astronomy and Astrophysics*, 20, 165
- Liu, R., Kliem, B., Titov, V. S., Chen, J., Wang, Y., Wang, H., Liu, C., Xu, Y., & Wiegmann, T. 2016, *The Astrophysical Journal*, 818, 148
- Lynch, B. J., Antiochos, S. K., DeVore, C. R., Luhmann, J. G., & Zurbuchen, T. H. 2008, *The Astrophysical Journal*, 683, 1192
- Moore, R. L. & Labonte, B. J. 1980, in *IAU Symposium*, Vol. 91, *Solar and Interplanetary Dynamics*, ed. M. Dryer & E. Tandberg-Hanssen, 207–210
- Moore, R. L. & Roumeliotis, G. 1992, in *Lecture Notes in Physics*, Berlin Springer Verlag, Vol. 399, *IAU Colloq. 133: Eruptive Solar Flares*, ed. Z. Svestka, B. V. Jackson, & M. E. Machado, 69
- Moore, R. L., Sterling, A. C., Hudson, H. S., & Lemen, J. R. 2001, *ApJ*, 552, 833
- Patsourakos, S., Vourlidas, A., Török, T., Kliem, B., Antiochos, S. K., Archontis, V., Aulanier, G., Cheng, X., Chintzoglou, G., Georgoulis, M. K., Green, L. M., Leake, J. E., Moore, R., Nindos, A., Syntelis, P., Yardley, S. L., Yurchyshyn, V., & Zhang, J. 2020, *SSRv*, 216, 131
- Qiu, J., Gary, D. E., & Fleishman, G. D. 2009, *Solar Physics*, 255, 107
- Qiu, J., Hu, Q., Howard, T. A., & Yurchyshyn, V. B. 2007, *ApJ*, 659, 758
- Qiu, J., Lee, J., Gary, D. E., & Wang, H. 2002, *ApJ*, 565, 1335
- Qiu, J., Wang, H., Cheng, C. Z., & Gary, D. E. 2004, *ApJ*, 604, 900
- Savcheva, A., Pariat, E., McKillop, S., McCauley, P., Hanson, E., Su, Y., & DeLuca, E. E. 2016, *ApJ*, 817, 43
- Song, H. Q., Zhang, J., Chen, Y., & Cheng, X. 2014, *The Astrophysical Journal*, 792, L40
- Titov, V. S., Hornig, G., & Démoulin, P. 2002, *J. Geophys. Res.*, 107, 1164
- Török, T., Downs, C., Linker, J. A., Lionello, R., Titov, V. S., Mikić, Z., Riley, P., Caplan, R. M., & Wijaya, J. 2018, *ApJ*, 856, 75
- Török, T. & Kliem, B. 2005, *ApJL*, 630, L97
- van Ballegooijen, A. A. & Martens, P. C. H. 1989, *ApJ*, 343, 971
- Wang, H., Qiu, J., Jing, J., & Zhang, H. 2003, *ApJ*, 593, 564
- Wang, W., Liu, R., Wang, Y., Hu, Q., Shen, C., Jiang, C., & Zhu, C. 2017, *Nature Communications*, 8, 1330
- Wang, Y., Zhuang, B., Hu, Q., Liu, R., Shen, C., & Chi, Y. 2016, *Journal of Geophysical Research: Space Physics*, 121, 9316
- Webb, D. F., Lepping, R. P., Burlaga, L. F., DeForest, C. E., Larson, D. E., Martin, S. F., Plunkett, S. P., & Rust, D. M. 2000, *J. Geophys. Res.*, 105, 27251
- Wyper, P. F., Antiochos, S. K., & DeVore, C. R. 2017, *Nature*, 544, 452
- Xing, C., Cheng, X., & Ding, M. 2020, *The Innovation*, 1, 100059
- Yan, X. L., Wang, J. C., Pan, G. M., Kong, D. F., Xue, Z. K., Yang, L. H., Li, Q. L., & Feng, X. S. 2018, *ApJ*, 856, 79
- Zhang, J., Dere, K. P., Howard, R. A., Kundu, M. R., & White, S. M. 2001, *ApJ*, 559, 452
- Zhong, Z., Guo, Y., & Ding, M. D. 2021, *Nature Communications*, 12, 2734
- Zhou, G. P., Tan, C. M., Su, Y. N., Shen, C. L., Tan, B. L., Jin, C. L., & Wang, J. X. 2019, *The Astrophysical Journal*, 873, 23
- Zhou, G. P., Zhang, J., & Wang, J. X. 2016, *The Astrophysical Journal*, 823, L19
- Zhu, C., Qiu, J., Liewer, P., Vourlidas, A., Spiegel, M., & Hu, Q. 2020, *The Astrophysical Journal*, 893, 141, arXiv: 2003.11134